Fermi National Accelerator Laboratory

FERMILAB-Pub-84/122-E
7190.497
(Submitted to Phys. Rev.)

CHARGED HYPERON PRODUCTION BY 400 GeV PROTONS

T. R. Cardello, P. S. Cooper, L. J. Teig, J. L. Thron, and Y. Wah
Yale University, New Haven, Connecticut 06520

and

C. Ankenbrandt, J. P. Berge, A. E. Brenner, J. Butler, K. Doroba,
J. E. Elias, J. Lach, P. Laurikainen, J. MacLachlan, and J. Marriner
Fermi National Accelerator Laboratory, Batavia, Illinois 60510

and

E. W. Anderson, A. Breakstone, and E. I. Rosenberg
Iowa State University, Ames, Iowa 50011

and

E. McCliment
University of Iowa, Iowa City, Iowa 52242

November 1984

Operated by Universities Research Association Inc. under contract with the United States Department of Energy

November 13, 1984

CHARGED HYPERON PRODUCTION BY 400 GeV PROTONS

T.R. Cardello*, P.S. Cooper, L.J. Teig, J.L. Thron†, Y. Wah††

Yale University, New Haven, Connecticut 06520

C. Ankenbrandt, J.P. Berge, A.E. Brenner, J. Butler, K. Doroba†,

J.E. Elias, J. Lach, P. Laurikainen**, J. MacLachlan, J. Marriner

Fermi National Accelerator Laboratory, Batavia, Illinois 60510

E.W. Anderson, A. Breakstone††, E.I. Rosenberg

Iowa State University, Ames, Iowa 50011

and

E. McCliment

University of Iowa, Iowa City, Iowa 52242

ABSTRACT

Differential production cross sections have been measured for Σ^-, Ξ^-, Ω^-, $\overline{\Sigma^-}$, $\overline{\Xi^-}$ and Σ^+ relative to pion production at several x_F and P_T with $.24 \leq x_F \leq .90$, and $P_T \leq 2$ GeV using 400 GeV protons incident on a Cu target. The data can be described by the function: $A \cdot (1 - x_F)^n e^{-B \cdot P_T}$, where A and n depend only on the hyperon type, and B is quadratic in x_F, and also depends on hyperon type. Comparison with previous experiments supports scaling in x_F over the range 200-400 GeV/c.

I. Introduction

We report here measurements of charged hyperon and anti-hyperon production over a broad range of Feynman x, x_F, and transverse momentum, P_T. The measurements were made in the Fermilab Proton Center charged hyperon beam[1] using 400 GeV protons incident on a copper target. A narrow-band charged-hyperon beam was tuned to momenta in the range of 100-360 GeV/c enabling us to explore the kinematic range $.24 \leq x_F \leq .90$ and $P_T \leq 2$ GeV/c. In this kinematic region, we describe the ratios of hyperon to pion production by the functional form

$$A \cdot (1-x_F)^n \cdot e^{-B(x_F) \cdot P_T} \qquad (1)$$

where A, n and B depend on the hyperon type and B is a quadratic function of x_F.

In section II of this paper, we describe the apparatus and trigger requirements for the various event topologies. Section III outlines the data reduction and analysis. Section IV describes the parameterization of the differential cross sections and compares our results with other, lower energy, measurements of hyperon production.

II. Apparatus and Trigger Logic

A plan view of the detector is shown in Fig. 1. A 400 GeV/c incident beam of between 10^9 and 10^{12} protons per 1 sec pulse was incident on a 14.8 x 0.2 x 0.2 cm^3 copper target. The primary beam had an angular divergence of .33 mrad full width half maximum (FWHM), and a spot size of less than 1 mm FWHM at the target. The charged secondary beam was defined by a curved tungsten channel with a radius of curvature of 350 m, turning the secondary beam through 21 mrad. The rectangular aperture of the channel which was varied along its length was 0.36 x 0.9 cm^2 at its downstream end. At its upstream end, the channel also served as a dump for the non-interacting primary beam. Both the target and channel were inside the field region of a 7.3 m magnet, the hyperon magnet. The channel and target are shown in Fig. 2. The resulting secondary beam had a full width momentum spread of $\Delta p/p = \pm 7\%$ and a solid angle of 0.64 μsr. The momentum of the secondary beam, and thus its production x_F, was varied by changing the field in the dump magnet. The transverse momentum of the secondaries was varied by changing the angle of the incident proton beam relative to that defined by the channel, using an angle varying bend magnet system.

Particles exiting the channel were required to be detected in a three scintillation counter beam telescope (B1, B2, B3). Particles outside the region defined by the channel were rejected by an additional pair of scintillators (VH1 and VH2). The locations of these counters are shown in Fig. 3.

High resolution proportional wire chambers[2] (PWCs) were used to measure the trajectories of the secondary particles. Positions were measured to better than 30 μm (rms) and the angles of the tracks were measured to within 50 μrad (rms). This information, when combined with the assumption that the particles originated in the target, resulted in a 0.7% (rms) momentum determination.

Downstream of the PWCs was an evacuated decay region 23 m long (10 m long for the 100 GeV/c data) followed by a drift chamber spectrometer. A four-section scintillator multiplicity counter (M) immediately upstream of this spectrometer served to identify events with more than one charged decay product. Using the magnetic drift-chamber spectrometer with a P_T of 0.84 GeV/c, the positions, angles and momenta of particles exiting the decay region was measured (rms) to within 150 μm, 100 μrad and 1% respectively.

Immediately downstream of this spectrometer, another magnet was used to provide additional momentum separation of the tracks. These tracks were further identified by the downstream trigger elements shown in Figs. 4 and 5. Events with a neutron decay were identified by an iron-scintillator calorimeter (NC) preceeded by a scintillation counter (NV). Two additional scintillators identified high momentum stable tracks (BV) and protons (P) consistent with Λ decay.

The events of interest fell into three classes. The broadest class was defined as a simple straight track in the high resolution PWCs, and required hits in B1, B2 and B3 and no hits

in VH1 and VH2. The topology of these "beam upstream" (BUPS) triggers is shown in Fig. 3.

The second class of events was designed to include candidates for the decays

$$\begin{array}{rl} & \Sigma^- \to n + \pi^- \\ \text{and} & \Xi^- \to \Lambda + \pi^- \\ & \qquad\;\; \hookrightarrow n + \pi^0. \end{array}$$

These events required an upstream beam particle (BUPS), no downstream beam particle ($\overline{BV}$), and the detection of a neutral particle ($NC \cdot \overline{NV}$). The topology of these "one track plus a neutral" (1TN) event is shown in Fig. 4. In the final data sample, we required both a single charged non-beam particle and a reconstructed vertex for an event to fall into this class.

The third class of events corresponded to a sequential decay, with two charged particles associated with the secondary vertex and one charged particle associated with the primary vertex. Events in this class were candidates for the decays:

$$\begin{array}{rl} & \Omega^- \to K^- + \Lambda \\ & \qquad\qquad\;\; \hookrightarrow p + \pi^- \\ \text{and} & \Xi^- \to \pi^- + \Lambda \\ & \qquad\qquad\;\; \hookrightarrow p + \pi^-. \end{array}$$

For an event of this class, we required an upstream beam particle (BUPS), signals from at least two quadrants of the multiplicity conter (M2), a proton signal (P) and no downstream stable beam particle ($\overline{BV}$). The topology of these three track

events (3T) is shown in Fig. 5.

A summary of the hyperon decay modes which were studied is given in Table I.

The geometrical acceptance of the apparatus for decays within the decay region of our detector was 100%, except for the shorter decay region used at 100 GeV/c. Here the acceptance fell to 90%. Triggering efficiency for Σ^- and Ξ^- (1TN events) decaying within the decay region was 77%. The short length of the neutron calorimeter was the primary cause of the trigger inefficiency. The 3T events, Ω^- and Ξ^-, which decayed in the decay region had a smaller triggering efficiency of 60%. For these 3T events, the primary loss of triggers was due to Λ decays downstream of the multiplicity counter.

III. Data Reduction and Analysis

The raw distribution of hits in the PWCs and drift chambers along with the trigger information was recorded on magnetic tape by a PDP 11/45 data acquisition computer. Offline a least-squares multi-track reconstruction algorithm was then applied to the data. Decays vertices were calculated from the fitted tracks and the differing decay hypotheses were imposed to calculate effective mass combinations. The events were then required to fall into one of the three classes (BUPS, 1TN, 3T) described previously. The various components of the secondary beam were identified as follows:

A. $\pi^{\pm}$

The charged pion signals were obtained from the non-decaying particles recorded with the BUPS trigger. To insure that these beam particles did not decay, the momentum of these tracks as measured independently by the PWCs and the drift chamber spectrometer were compared. Figure 6 shows a plot of the residuals variable

$$\zeta = \frac{\Sigma \Delta_i}{\partial \Delta_i} \qquad (2)$$

where Δ_i is the difference in the i^{th} component of the momentum vector as measured by the PWCs and the drift chamber spectrometer and $\partial\Delta_i$ is the rms resolution in Δ_i. By demanding ζ lies within 4 standard deviations (4σ) of the mean of this distribution we

identify particles that do not decay within the decay volume of the apparatus. The known production cross-sections[3] can then be used to infer the number of charged pions within this sample. All of our subsequent particle yields are given relative to pion production. Thus, the uncertainties in the pion production cross sections introduce a systematic error in our results on hyperon production.

All of the hyperon event candidates were identified by requiring at least one reconstructed vertex. In addition to the probability requirements imposed during track and vertex reconstruction, several additional requirements were imposed. (1) Non-decaying beam particles were eliminated by imposing a minimum transverse momentum requirement on the charged decay meson. This requirement also improved the decay vertex resolution. (2) All reconstructed vertices were required to lie within the vacuum decay region. This requirement reduced the background due to particle interactions. (3) For each hypeeron an appropriately restricted mass[4] region was studied. (4) For the 100 GeV data, 1TN class events which had a fit consistent with the hypothesis

$$\begin{array}{llll} K^{\pm} & \rightarrow & \pi^{0} & + \ \pi^{\pm} \\ & & | & \\ & & \rightarrow & \gamma + \gamma \end{array}$$

were eliminated. At this energy, $K^{\pm}$ is a significant source of background to the Σ^{+} and Σ^{-} signals and must be eliminated. Table II summarizes these criteria and others to be described below.

B. Σ^-, Ξ^-, AND $\overline{\Xi^-}$

The Σ^-, Ξ^-, and $\overline{\Xi^-}$ signals were obtained from events in the 1TN class, assuming the decays

$$\Sigma^- \rightarrow n + \pi^-$$

$$\begin{array}{l}\Xi^- \rightarrow \Lambda + \pi^- \\ \qquad\quad \lfloor\!\!\rightarrow n + \pi^0\end{array}$$

$$\begin{array}{l}\overline{\Xi^-} \rightarrow \Lambda + \pi^+ \\ \qquad\quad \lfloor\!\!\rightarrow n + \pi^0 .\end{array}$$

The appropriate two-body effective mass distributions are shown in Figs. 7-9. In each case, the mass distribution was fit to a Gaussian peak plus a linear background term. Table III summarizes these fitting functions. The number of hyperons was defined as those events within 4σ of the mean effective mass of the peak less the integral of the background term over this mass region.

C. Σ^+ and $\overline{\Sigma^-}$

The 1TN class of events is also a source of candidates for the decays

$$\Sigma^+ \rightarrow n + \pi^+$$

$$\overline{\Sigma^-} \rightarrow \bar{n} + \pi^+.$$

The π^+ + (neutrals) effective mass at x_F = 0.27 is plotted in Fig. 10. Since the $\Sigma^+ - \overline{\Sigma^-}$ mass difference (8 MeV) is less than twice our effective mass resolution (4.5 MeV), we fit this data to two Gaussian peaks plus a linear background term. The Gaussians were constrainted to have the same width and a fixed separation of 8 MeV. The total number of Σ^+ and $\overline{\Sigma^-}$ was defined as the total number of events in the plot less the integral of the background term. The relative number of $\Sigma^+/\overline{\Sigma^-}$ was defined as the ratio of the amplitudes of the fitted Gaussians.

A further test of the two peak hypothesis for the π^+ + (neutral) effective mass plot is based on the $\Sigma^+/\overline{\Sigma^-}$ lifetime difference. Requiring the decay vertex to lie in the upstream half of the decay region enhances the Σ^+ signal; requiring vertices in the downstream half enhances the $\overline{\Sigma^-}$ signal. Figure 11 superimposes the π^+ + (neutral) effective mass plots for these two requirements. The plots are normalized to the same number of events and show the anticipated mass shift.

D. Ω^-

The events in the 3T class are candidates for the decays

$$\begin{array}{l} \Omega^- \rightarrow \Lambda + K^- \\ \qquad\quad \lfloor\!\rightarrow p + \pi^- \end{array}$$

$$\begin{array}{l} \Xi^- \rightarrow \Lambda + \pi^- \\ \qquad\quad \lfloor\!\rightarrow p + \pi^- \end{array}$$

The Λ is identified using two of the tracks in the drift chamber spectrometer. The ΛK^- and $\Lambda\pi^-$ mass hypotheses are then used to distinguish the Ω^-s from the Ξ^- background. Figure 12 is a scatter plot of the two effective mass combinations. For both the Ω^- and Ξ^- yields, the density of non-resonant points within the respective mass bands is assumed to be the same as that outside the bands. The Ω^- events are defined as those with $M_{\Lambda\pi^-} \geq 1.341$ GeV and $1.656 \leq M_{\Lambda K^-} \leq 1.688$ GeV.

While not used in quoting Ξ^- yields, the number of Ξ^- events obtained from the 3T class can be compared with that obtained from the 1TN class. To within the statistical accuracy of the data, the yields are identical. Thus we are confident that the relative acceptance for the two events classes is well understood. This enables us to combine ratios $(\Omega^-/\Xi^-)_{3T}$ and $(\Xi^-/\pi^-)_{1TN}$ in obtaining the relative Ω^- to π^- yields.

The hyperon yields at the production target are determined from the number of hyperons observed in the various mass plots. We apply corrections for various loss mechanism: reabsorption in the target, upstream decays, trigger inefficiency, geometric acceptance and reconstruction inefficiency. The uncertainty in the yields due to applying these corrections is less than 5%. Most of our results are expressed in terms of relative yields so that dependence on the channel acceptance is minimized. In addition, by comparing particles in the same trigger class and with similar topologies we minimize the dependence on trigger and

reconstruction inefficiencies. This reduces the errors on the relative yields. A summary of the yield results is given in Table IV.

IV. Results

We represent our hyperon to pion production ratios in the QCD motivated form[8] of equation (1).

We determine the function $B(x_F)$ by fitting the data to the form $C \cdot e^{-BP_T}$ at each measured value of x_F. From the variation of B with x_F, we find $B(x_F)$ can be described as a quadratic polynomial in x_F for each hyperon studied.

The ratios are then fit to the function

$$f = a_1 \cdot (1-x_F)^2 \cdot e^{-P_T(a_3+a_4 \cdot x_F+a_5 \cdot x_F^2)}. \qquad (3)$$

Figures 13 through 15 show the ratios measured as a function of P_T along with the fitted function f. Table V gives our fits to the parameters a_1 through a_5 for each measured ratio. Using these fitted parameters, the ratios are calculated at $P_T=0$, yielding the solid curves shown in Figures 16 and 17.

Also shown in Figures 16 and 17 are our measurements of these production ratios. We plot only the extreme values as a function of x_F and indicate the P_T region in which these measurements are made. For comparison with non-strange baryon production, we have scaled the measurements[9] of p/π^+ at 400 GeV/c to a beryllium target containing the same number of interaction lengths as our copper target. In all cases, we note the sharp rise of the hyperon to pion yield as a function of x_F.

To compare our data to lower energy measurements[5,6,7] of charged hyperon production, we extrapolate our fits of the relative hyperon to pion production to $P_T=0$. The absolute hyperon production cross sections are obtained by combining these extrapolations with the pion invariant cross sections as parameterized in Reference 5. In Fig. 18, we plot the 1σ extent of these absolute cross sections along with the lower energy data. In the region of overlap, our extrapolated fit well represents the measurements of Bourquin *et al.*[5] and supports x_F scaling in the energy regime 200-400 GeV/c. Neither of the high energy experiments scales with the 20-30 GeV/c data[6,7]. The leading particle effect is evident in the rather slow decrease in $E\frac{d^3\sigma}{dp^3}$ as a function of x_F. It is also apparent in the change in slope when comparing Ξ^- to Σ^- production.

ACKNOWLEDGEMENTS

We wish to thank the staff of Fermilab, and particularly the Proton, Physics and Computing Departments for their aid in completing this experiment. This work was supported in part by the U.S. Department of Energy under contracts number DE-AC-02-76-CHO-3000, and DE-AC-02-76-ERO-3075 and W-7405-ENG-82-KA-01-01.

REFERENCES

* Present Address: 159 Islington St., Staten Island, NY, 10308.

† Present Address: High Energy Physics Division, Argonne National Laboratory Argonne, IL 60439.

++ Present Address: Enrico Fermi Institute, University of Chicago Chicago, IL 60637.

+ Present Address: Institute of Physics, Warsaw University, Warsaw, Poland.

** Present Address: Department of High Energy Physics University of Helsinki, Helsinki, Finland.

†† Present Address: Department of Physics University of Hawaii Honolulu, HI 96822.

1. T.R. Cardello, Fermilab TM-964(1984); T.R. Cardello, thesis submitted to Yale University (1983).

2. W. Freize, et al., Nucl. Instr. Meth. 136, 93 (1976).

3. J.R. Johnson, et al., Phys. Rev. D17, 1292 (1978); A.E. Brenner, et al., Phys. Rev. D26, 1497 (1982); D. Cutts, et al., Phys. Rev. Lett. 40, 141 (1978); C. Bromberg, et al., Nucl. Phys. B107, 82 (1976); W.F. Baker, et al., Phys. Lett. 51B, 303 (1974).

4. Here and throughout the masses, branching ratios and lifetimes used are from Particle Data Group, Phys. Lett. 111B (1982).

5. M. Bourquin, et al., Nucl. Phys. B153, 13 (1979).

6. V. Hungerbuhler, et al., Phys. Rev. D12, 1203 (1975).

7. J. Badier, et al., Phys. Lett. 39B, 414 (1972).

8. J. Gunion, Phys. Rev. D10, 242 (1974);
S. Brodsky and J. Gunion, Phys. Rev. D17, 848 (1978);
J. Gunion, Proc. Europhysics Study Conf., Erice, Italy, 293 (1981).

9. H. W. Atherton, et al., "Precise Measurements of Particle Production by 400 GeV/c Protons on Beryllium Targets," CERN 80-07, Geneva, Switzerland, 1980.

Table I: Hyperons and decay modes studied. Anti-hyperons and their decay products are studied for all modes except 1) and 6).

	DECAY	BRANCHING RATIO
1)	$\Sigma^+ \rightarrow n + \pi^+$	0.48
2)	$\Sigma^- \rightarrow n + \pi^-$	1.00
3)	$\Xi^- \rightarrow \Lambda + \pi^-$	1.00
	$\rightarrow n + \pi^\circ$	0.35
4)	$\Xi^- \rightarrow \Lambda + \pi^-$	1.00
	$\rightarrow p + \pi^-$	0.64
5)	$\Omega^- \rightarrow \Lambda + k-$	0.68
	$\rightarrow p + \pi^-$	0.64
6)	$\Omega^- \rightarrow \Xi^\circ + \pi^-$	0.23
	$\rightarrow \Lambda + \pi^\circ$	1.00
	$\rightarrow p + \pi^-$	0.64

Table II: Cuts and tolerances applied to the data. The cut number code is as follows:

1) Minimum P_T of meson from beam vertex
2) Minimum vertex z
3) Maximum vertex z
4) Number of standard deviations in fit integration limits
5) Reject events within this tolerance of K^+ mass
6) Maximum momentum non-conservation of decays
7) Minimum mass calculated using $\Lambda\pi^-$ hypothesis

CUT	1T NEGATIVE BEAM		1T POSITIVE BEAM		3T ONLY	
NO.	<160 GeV	>160 GeV	<160 GeV	>160 GeV	<160 GeV	>160 GeV
1	.0188 GeV	0.028 GeV	0.032 GeV	0.032 GeV	0.0188 GeV	0.0188 GeV
2	361.2 cm	450.0 cm	261.2 cm	311.2 cm	261.2 cm	261.2 cm
3	1337.8 cm	2602.8 cm	1187.8 cm	2452.2 cm	1187.8 cm	2602.8 cm
4	4	4	8	8	4	4
5			0.02 GeV			
6					0.02	0.02
7					1.341 GeV	1.341 GeV

Table III: Decay modes and fit functions. The a_i are the fitted parameters. m is the hyperon mass assuming the stated decay mode. Anti-particles are treated in the same manner as particles unless explicitly stated.

DECAY MODE	FITTED FUNCTION
$\Sigma^- \rightarrow n + \pi^-$	F′
$\Xi^- \rightarrow \Lambda + \pi^-$	
$\rightarrow n + \pi^0$	F
$\Xi^- \rightarrow \Lambda + \pi^-$	
$\rightarrow p + \pi^-$	F
$\Omega^- \rightarrow \Lambda + k^-$	
$\rightarrow p + \pi^-$	None
$\Sigma^+ \rightarrow n + \pi^+$	F+G
$\overline{\Sigma^-} \rightarrow \bar{n} + \pi^+$	F+G

FUNCTIONS

$$F = a_1 + a_2 m + a_3/(a_4\sqrt{2\pi}) \exp\left\{-(m-a_5)^2/(2a_4^2)\right\}$$

$$F' = F + a_6/(2a_4\sqrt{2\pi}) \exp\left\{-(m-a_5)^2/(8a_4^2)\right\}$$

$$G = a_6/(a_4\sqrt{2\pi}) \exp\left\{-(m-a_5-\delta)^2/(2a_4^2)\right\}$$

δ = $\overline{\Sigma^-}$ - Σ^+ mass difference

Table IV: Measured production ratios at the target. The errors listed are statistical (systematic). The * denotes an average over a wide range of P_T. For the Σ^+ for $x_F >$ 0.6 no correction has been made for contributions from $\overline{\Sigma^-}$.

a. Σ^-/π^-

x_F	P_T	RATIO	ERROR
.90±.03	.37±.12	7.03	.30 (.90)
.89±.03	.49±.12	4.68	.20 (.60)
.78±.03	.35±.10	3.50	.16 (.06)
.77±.03	.40±.10	2.71	.14 (.04)
.76±.03	1.11±.11	1.62	.11 (.03)
.67±.03	.31±.09	1.05	.025(.010)
.67±.02	.10±.09	1.02	.055(.010)
.66±.03	.94±.09	.938	.031(.009)
.66±.03	1.27±.10	.946	.047(.009)
.54±.02	.28±.07	.284	.032(.003)
.53±.02	.23±.07	.387	.027(.004)
.53±.02	.72±.07	.510	.027(.005)
.39±.01	.01±.05	.123	.024(.000)
.27±.01	.21±.04	.069	.010(.000)
.27±.01	.01±.04	.064	.011(.000)
.27±.01	.37±.04	.086	.019(.000)
.27±.01	.51±.04	.077	.017(.000)

b. Ξ^-/π^-

.90±.03	.37±.12	.0574	.0098(.0074)
.89±.03	.49±.12	.0360	.0058(.0046)
.77±.03	.40±.10	.060	.032 (.001)
.76±.03	1.11±.11	.091	.021 (.001)
.68±.03	.32±.09	.0531	.0029(.0005)
.67±.03	.10±.09	.0339	.0041(.0003)
.67±.03	.94±.10	.0616	.0036(.0006)
.66±.03	1.27±.10	.0830	.0057(.0008)
.54±.02	.28±.07	.0196	.0025(.0002)
.54±.02	.23±.07	.0302	.0030(.0003)
.53±.02	.72±.08	.0501	.0047(.0005)
.40±.02	.01±.05	.0192	.0040(.0002)
.28±.01	.21±.04	.0120	.0019(.0000)
.28±.02	.37±.04	.0139	.0033(.0000)
.28±.01	.01±.04	.0113	.0020(.0000)
.27±.01	.01±.04	.0117	.0026(.0000)

c. Ω^-/π^-

.90±.03	.43*	.56E-3	(.56E-3)
.77±.03	.52*	.86E-3	(.86E-3)
.67±.03	1.22±.10	.122E-2	.17E-3(.1E-4)
.67±.03	.95±.10	.102E-2	.16E-3(.1E-4)
.67±.03	.33±.09	.470E-3	.65E-4(.5E-5)
.67±.03	.10±.09	.59E-3	.23E-3(.6E-5)
.67±.03	.24±.09	.78E-3	.16E-3(.9E-5)
.54±.02	.28±.07	.17E-3	.12E-3(.2E-5)
.54±.02	.23±.07	.109E-2	.48E-3(.1E-4)
.54±.02	.73±.08	.164E-2	.45E-3(.2E-4)
.27±.01	.23*	.35E-3	(.25E-3)

d. Σ^+/π^+

.78±.03	1.46±.12	3.26	.35 (.82)
.77±.03	2.15±.13	3.35	.60 (.84)
.77±.03	1.00±.11	2.09	.49 (.53)
.64±.02	.84±.09	.78	.16 (.14)
.64±.02	1.21±.10	1.00	.17 (.18)
.54±.02	1.01±.08	.371	.040(.046)
.53±.02	.69±.08	.235	.031(.030)
.53±.02	.55±.07	.260	.031(.032)
.52±.02	1.42±.09	.323	.039(.041)
.27±.01	.81±.05	.071	.022(.003)
.26±.01	.57±.04	.065	.019(.003)
.26±.01	.51±.04	.081	.023(.004)
.26±.01	.01±.03	.065	.014(.003)
.26±.01	.20±.04	.059	.017(.003)

e. $\overline{\Sigma^-}/\pi^+$

.54±.02	1.01±.08	.141E-1	.18E-2(.17E-2)
.53±.02	.69±.08	.69E-2	.18E-2(.8E-3)
.53±.02	.55±.07	.89E-2	.18E-2(.11E-2)
.52±.02	1.42±.09	.154E-1	.24E-2(.2E-3)
.27±.01	.81±.05	.40E-2	.12E-2(.2E-3)
.26±.01	.57±.04	.355E-2	.96E-3(.16E-3)
.26±.01	.51±.04	.55E-2	.14E-2(.2E-3)
.26±.01	.01±.03	.381E-2	.71E-3(.17E-3)
.26±.01	.20±.04	.358E-2	.91E-3(.15E-3)

f. $\overline{\Xi^-}/\pi^+$

.27±.01	.81±.05	.156E-2	.56E-3(.4E-4)
.26±.01	.57±.04	.84E-3	.45E-3(.4E-4)
.26±.01	.51±.04	.171E-2	.62E-3(.7E-4)
.26±.01	.01±.03	.122E-2	.45E-3(.5E-4)
.26±.01	.20±.04	.129E-2	.51E-3(.8E-4)

Table V: Fit results for the function $a_1 \cdot (1-x_F)^{a_2} \cdot e^{-P_T(a_3+a_4 \cdot x_F+a_5 \cdot x_F^2)}$. The χ^2/NDF is the fit χ^2 per degree of freedom.

RATIO	a_1	a_2	a_3	a_4	a_5	χ^2/NDF
Σ^-/π^-	0.0194±0.0024	-3.60±0.11	0.45±0.84	-7.5±2.5	10.3±2.0	19/12
Ξ^-/Σ^-	0.379 ±0.025	2.10±0.11	0.87±0.48	-0.8±2.0	-2.2±1.6	12/11
Ξ^-/π^-	0.0077±0.0012	-1.33±0.17	4.6 ±1.1	-22.2±3.7	21.3±3.2	19/11
Ω^-/Ξ^-	0.047 ±0.039	1.42±0.77	-0.46±0.14			10/5
Ω^-/Σ^-	0.0069±0.0061	2.66±0.82	-1.15±0.16			10/5
Ω^-/π^-	0.0001±0.0001	-1.5 ±1.0	-0.94±0.17			10/5
Σ^+/π^+	0.0245 ±0.0027	-2.88±0.16	-0.35±0.12			8/11
$\overline{\Sigma^-}/\pi^+$	0.00187±0.00036	-1.65±0.40	-0.59±0.21			8/6
$\overline{\Sigma^-}/\Sigma^+$	0.0824 ±0.0058	1.13±0.20	-0.09±0.11			6/6
$\overline{\Xi^-}/\pi^+$	0.00120±0.00037		-0.08±0.64			2/3
$\overline{\Xi^-}/\Sigma^+$	0.0182 ±0.0032		0.±0.34			2/3
$\overline{\Xi^-}/\overline{\Sigma^-}$	0.318 ±0.056		0.02±0.35			2/3
Σ^+/p	0.0310 ±0.0035	-0.38±0.16	-0.35±0.013			8/11

FIGURE CAPTIONS

Fig. 1. Plan view of the experimental arrangement. Note the scales, different in x and z, are indicated in meters.

Fig. 2. Momentum selecting channel. (Not to scale.) The non-interacting beam is dumped in the enlarged upstream section of the channel.

Fig. 3. Plan view of the apparatus defining the non-decaying trajectory. The scale is given in meters. Trigger scintillation counters B1, B2 and B3 and also halo veto counters VH1 and VH2 defined an incident particle. Beam veto (BV) identified a non-interacting, non-decaying particle. For the beam upstream (BUPS) trigger only, the upstream scintillators are used. The non-decaying beam profile is shown downstream.

Fig. 4. The 1TN trigger type is defined by an BUPS trigger and a neutral particle hitting the neutron calorimeter (NC), preceded by a neutral veto (NV) and the non-decaying beam veto (BV). The most downstream magnet steers charged decay products away from the neutron counter and beam veto. Decay product profiles are shown downstream. Trigger 1TN is sensitive to decay modes 1), 2) and 3) in

Table I. Scale is shown in meters.

Fig. 5. The three particle trigger type 3T is defined by a BUPS and two or more of the multiplicity counters and P and not BV. Trigger 3T is sensitive to decay modes 4), 5) and 6) in Table I. Decay product profiles are shown downstream. Scale is shown in meters.

Fig. 6. A histogram of the residuals (ζ), representing the difference in momentum measured in the PWCs and in the drift chamber spectrometer, relative to the rms resolution of the momentum measurements for non-decaying beam particles.

Fig. 7. The measured Σ^- mass distributions. In this distribution, there are 24471 entries. Of these after subtracting background, there are 24294±191 Σ^- events.

Fig. 8. The measured Ξ^- mass distribution. The range of this histogram was chosen to minimize the background from the Σ^-. There are 709 entries in this histogram, of which 642±35 are Ξ^- events.

Fig. 9. A histogram of the $\overline{\Xi^-}$ mass. In this distribution, there are 359 entries. Of these, 136±30 are estimated to be $\overline{\Xi^-}$ over a background of 223±24 events.

Fig. 10. The effective mass for π^+ + (neutrals) at 100 GeV/c incident momentum an $x_F = 0.27$. These represent the Σ^+ and $\overline{\Sigma^-}$ sample plus background. Shown are 1895 entries with 1.0 MeV bin width. The fits described in the text results in 703±50 Σ^+, 643±50 $\overline{\Sigma^-}$ and 549±33 background events.

Fig. 11. The Σ^+ and $\overline{\Sigma^-}$ mass histogram divided into first and second half of the decay fiducial volume. In order to see that Fig. 10 is composed of two distinct signals, events which decay in the second half of the decay volume are removed from Fig. 10 and the result shown by the solid histogram. The $\overline{\Sigma^-}$ signal is thereby reduced relative to the Σ^+. Events which decay in the first half of the decay volume are removed from Fig. 10 and the area normalized result is shown by the dashed histrogram. The $\overline{\Sigma^-}$ signal is thereby enhanced relative to the Σ^+.

Fig. 12. The effective scatterplot mass $\Lambda\pi^-$ vs. ΛK^- for the 3T class representing Ξ^- and Ω^- candidates respectively.

Fig. 13. The Σ^-/π^- production ratios as a function of P_T at a number of x_F. The fitted function f is also shown.

Fig. 14. The Ξ^-/π^- and Ω^-/π^- production ratios as a function of P_T. The fitted function f as described in the text is also shown.

Fig. 15 Production ratios Σ^+/π^+, $\overline{\Sigma^-}/\pi^+$ and $\overline{\Xi^-}$ as a function of P_T. The fitted functions f are also shown.

Fig. 16. The production ratios Σ^-/π^-, Ξ^-/π^- and Ω^-/π^- as a function of x_F. For each value of x_F, the extreme values as measured by this experiment are plotted and the P_T value of the measurement indicated. The solid lines represent the P_T=0 fits of equation (3). Also plotted is the production ratio p/π^+ reported in Reference 9 corrected for target differences as described in the text.

Fig. 17. The production ratios Σ^+/π^+, $\overline{\Sigma^-}/\pi^+$, and $\overline{\Xi^-}/\pi^+$ as a function of x_F. For each value of x_F, the extreme values as measured by this experiment are plotted and the P_T value of the measurement indicated. The solid lines represent the P_T=0 fits of equation (3). Also plotted is the production ratio p/π^+ reported in Reference 9 corrected for target differences as described in the text.

Fig. 18. The invariant cross-section for charged hyperon production at low P_T. The data of this experiment is extrapolated to $P_T=0$ and normalized to the pion cross section as described in the text. The bands represent the 1σ extent of this extrapolation. Also plotted are the corresponding data from References 5-7.

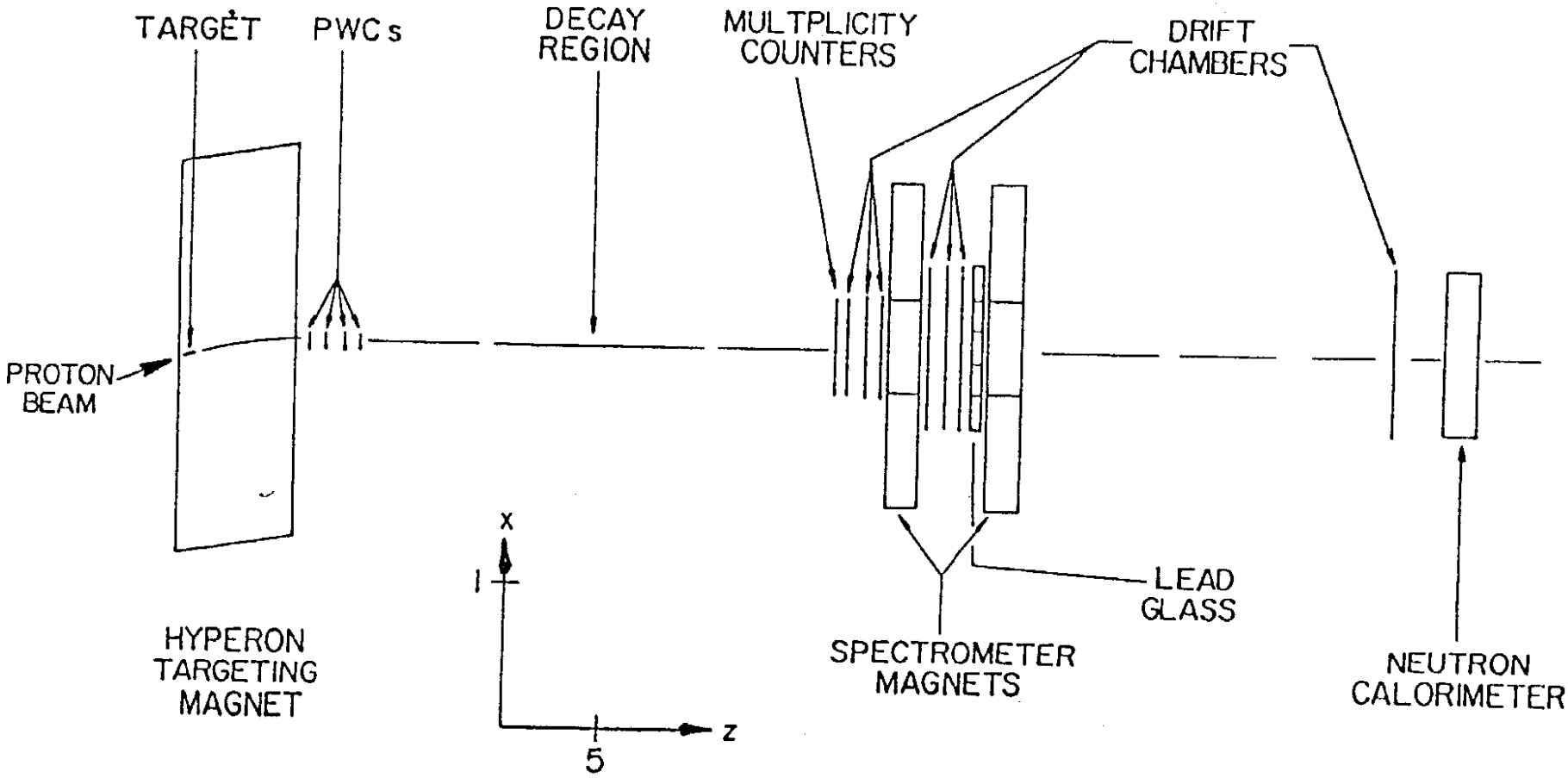
TARGET
PWCs
DECAY REGION
MULTPLICITY COUNTERS
DRIFT CHAMBERS
PROTON BEAM
HYPERON TARGETING MAGNET
X
1
5
Z
LEAD GLASS
SPECTROMETER MAGNETS
NEUTRON CALORIMETER

Fig. 1

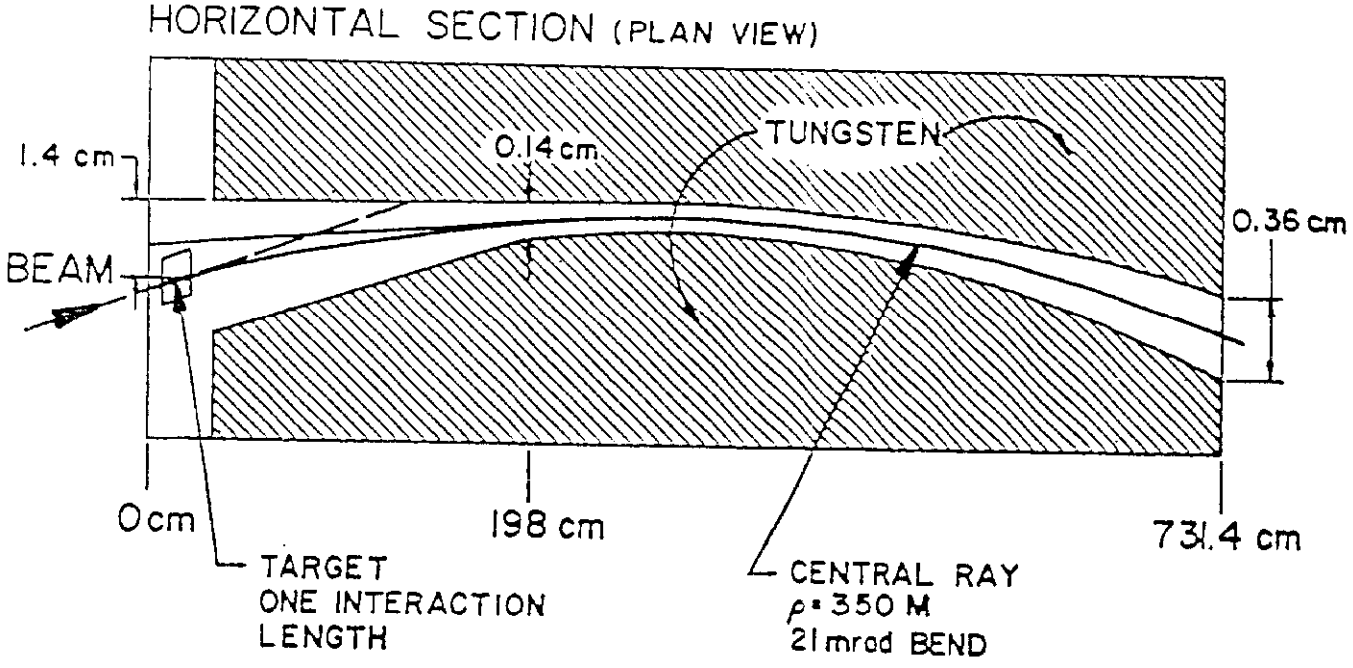
HORIZONTAL SECTION (PLAN VIEW)
1.4 cm
0.14 cm
TUNGSTEN
0.36 cm
BEAM
0 cm
198 cm
731.4 cm
TARGET
ONE INTERACTION
LENGTH
CENTRAL RAY
ρ = 350 M
21 mrad BEND

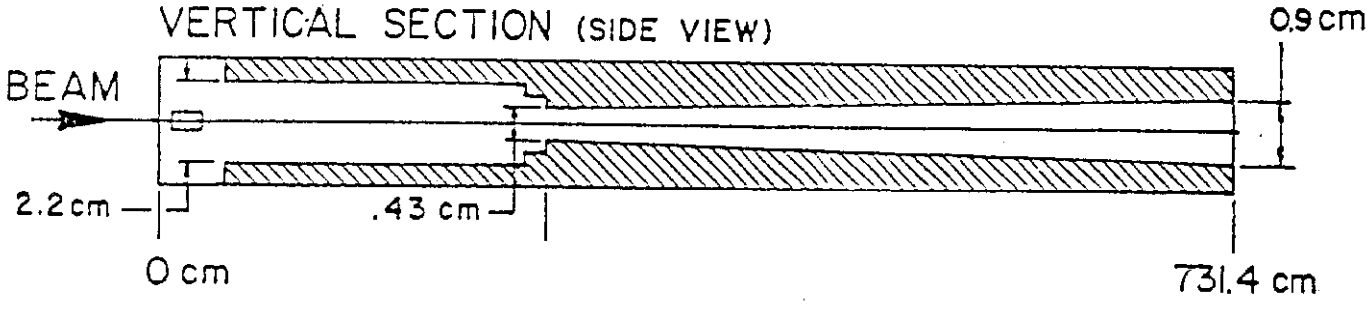
VERTICAL SECTION (SIDE VIEW)
0.9 cm
BEAM
2.2 cm
.43 cm
0 cm
731.4 cm

Fig. 2

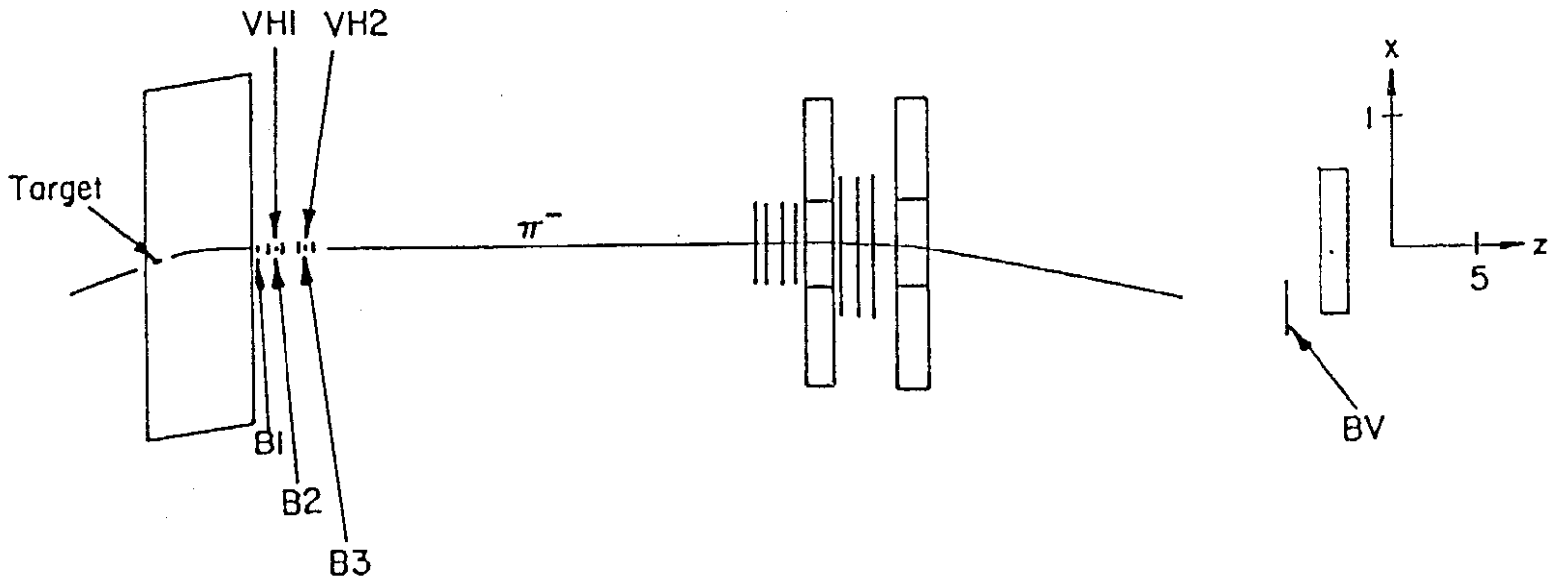

$$BUPS = B2 \cdot B1 \cdot B3 \cdot \overline{(VH1 + VH2)}$$

Fig. 3

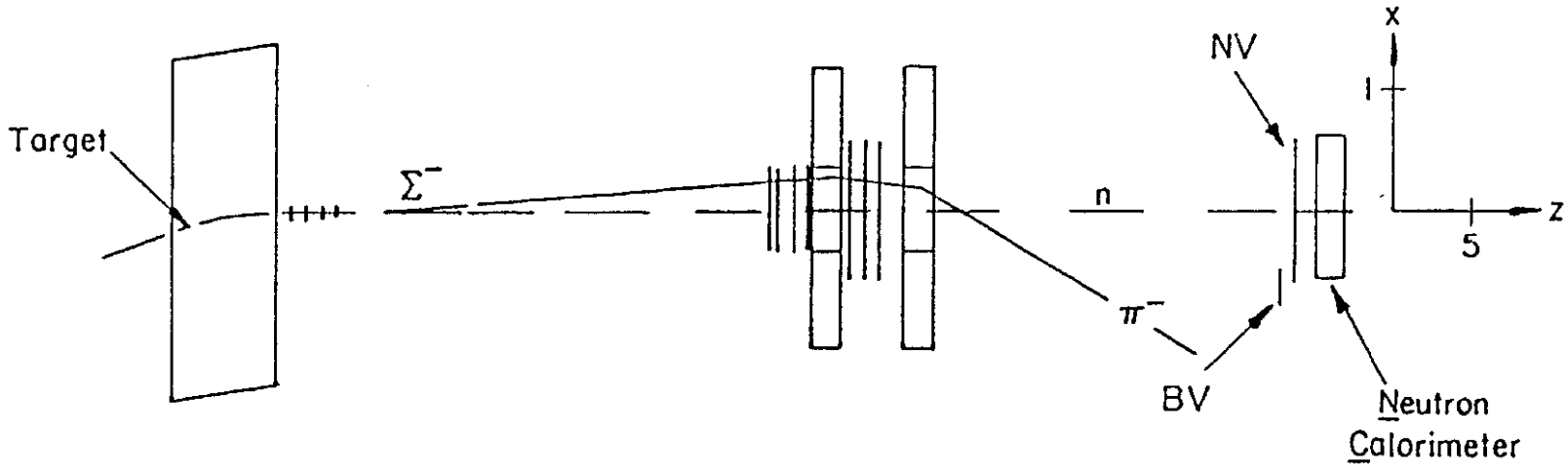

$$ITN = BUPS \cdot NC \cdot \overline{NV} \cdot \overline{BV}$$

Fig. 4

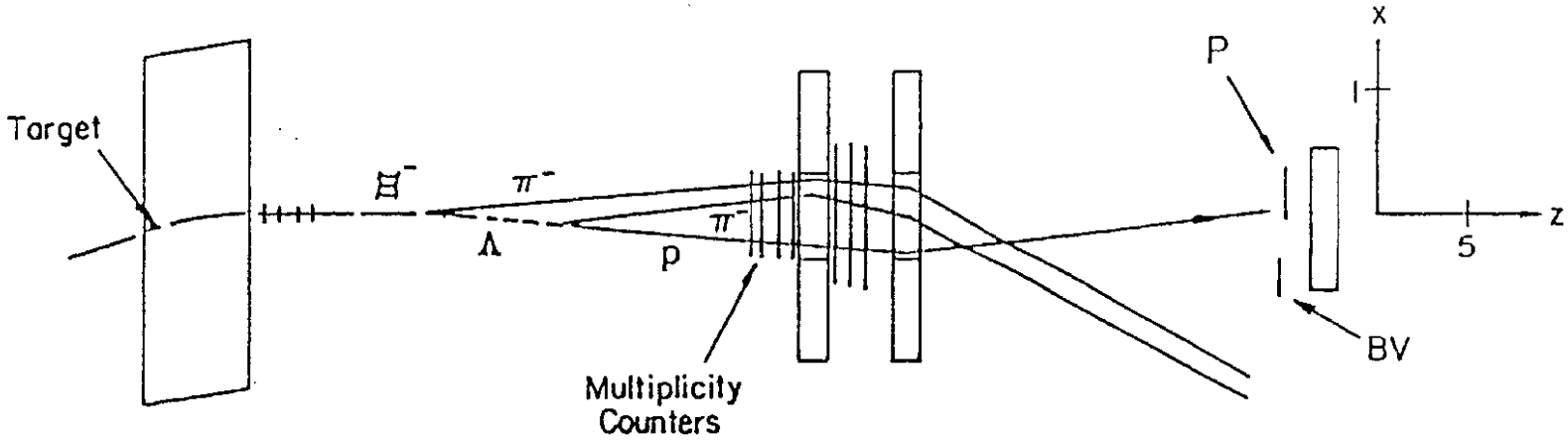

$$3T = BUPS \cdot M2 \cdot P \cdot \overline{BV}$$

Fig. 5

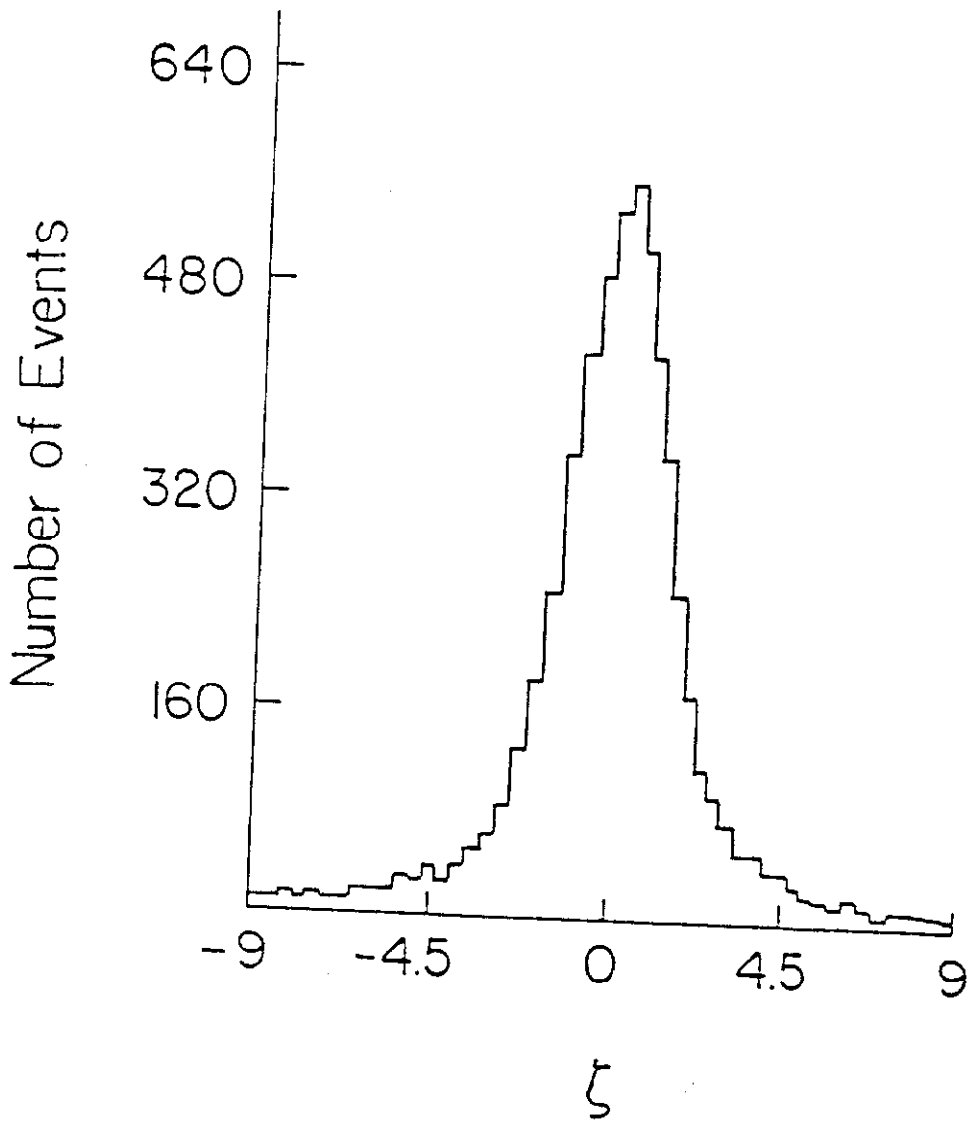

Fig. 6

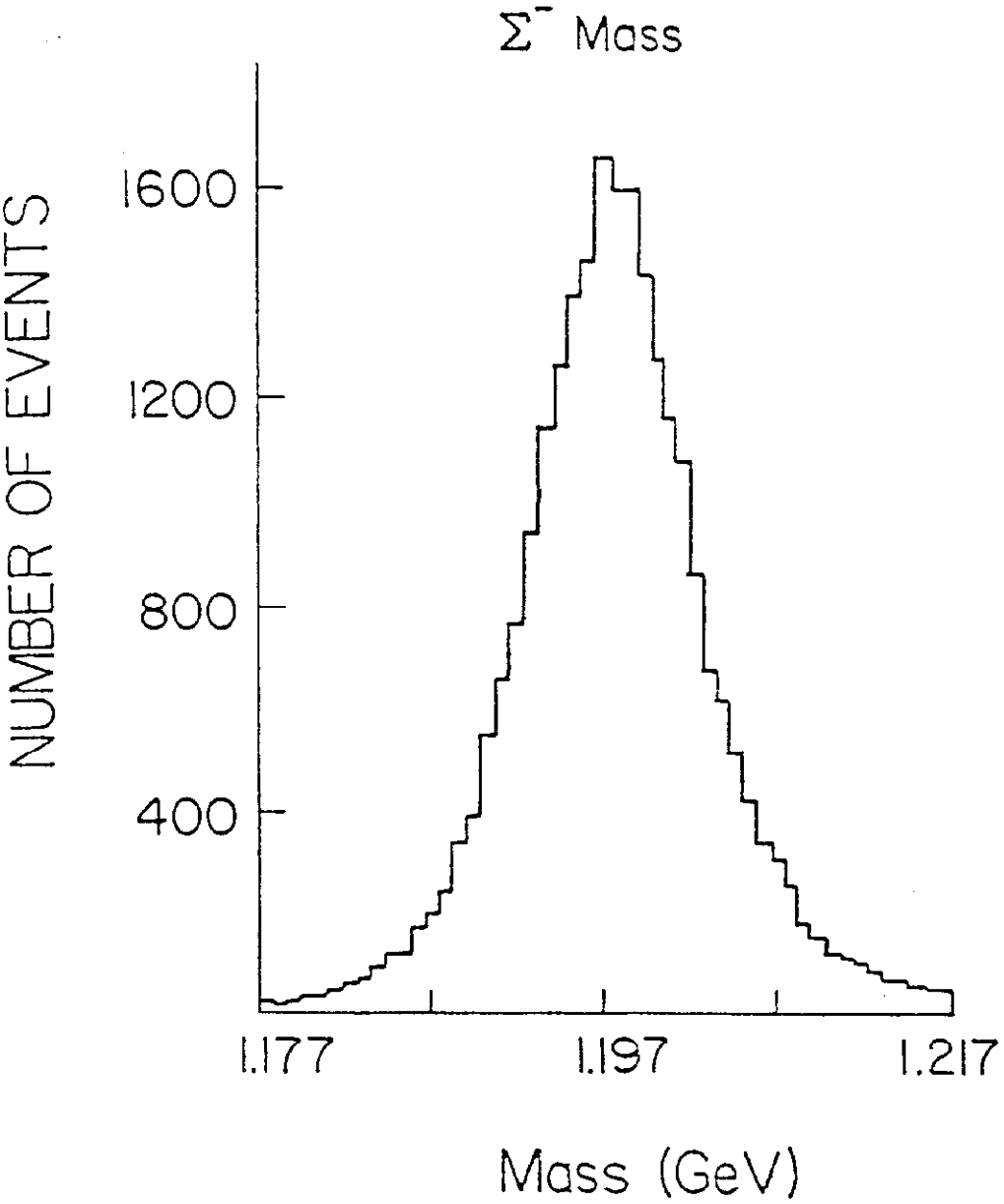
Σ^- Mass
NUMBER OF EVENTS
1600
1200
800
400
1.177
1.197
1.217
Mass (GeV)

Fig. 7

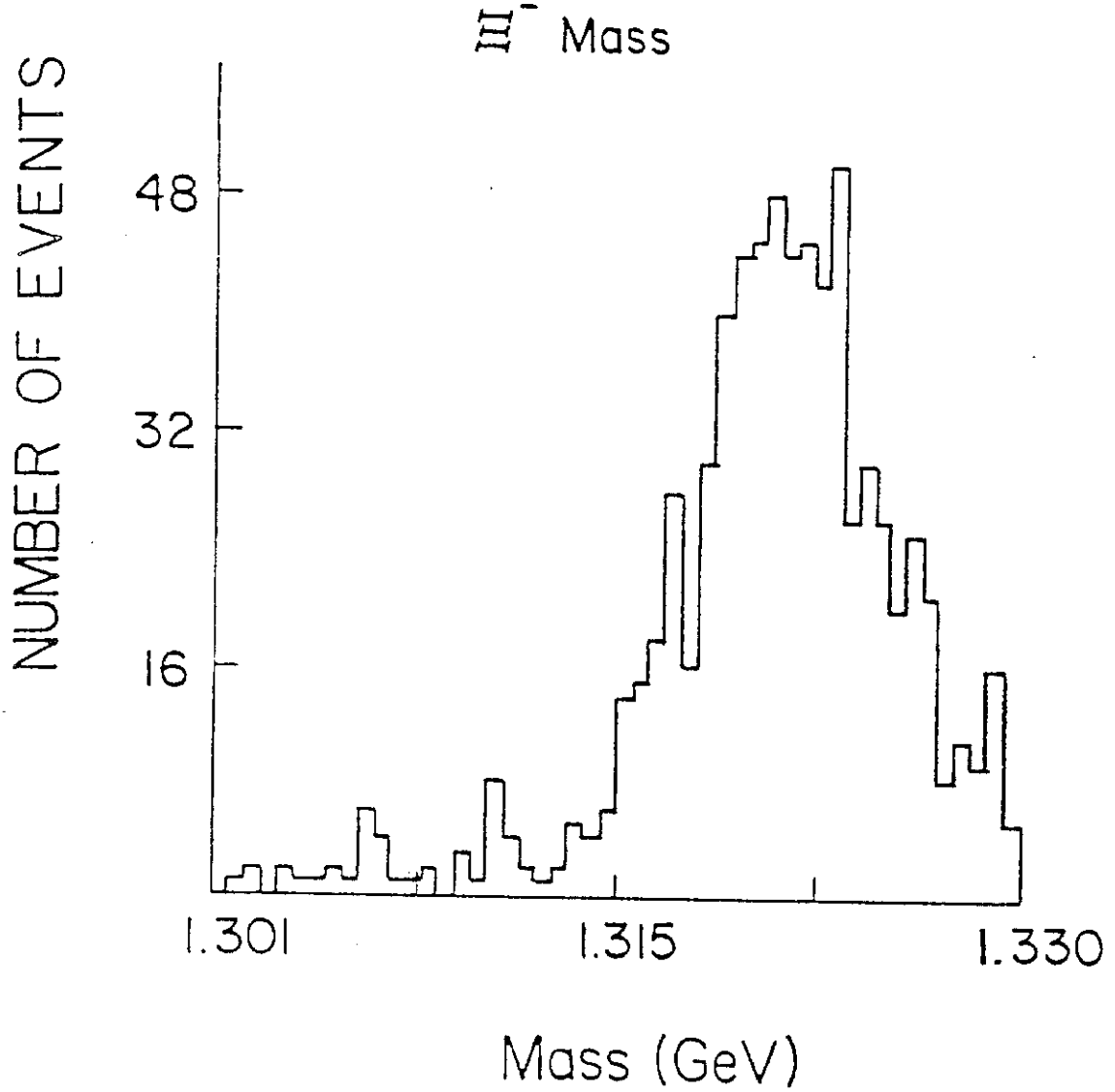

Fig. 8

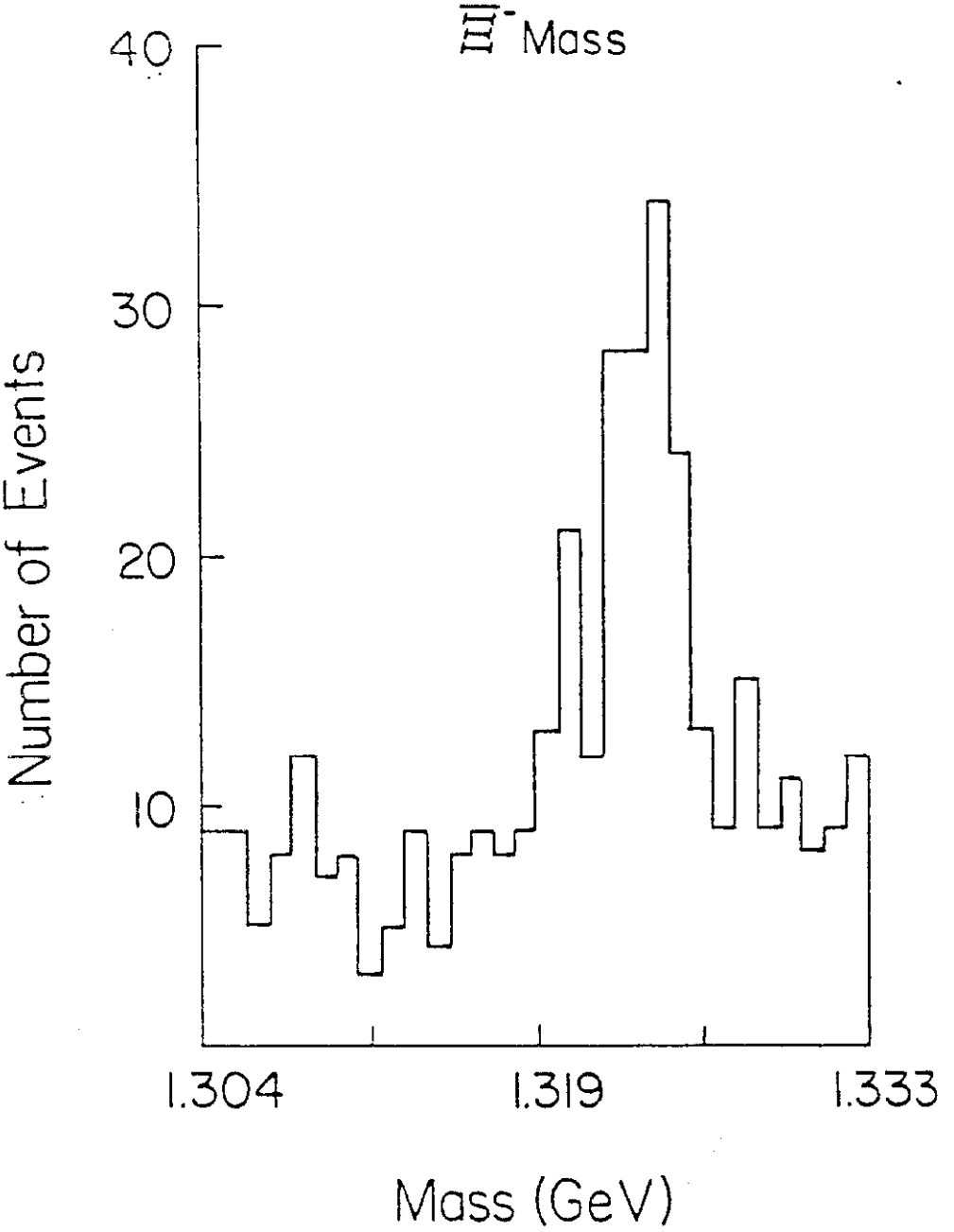

Fig. 9

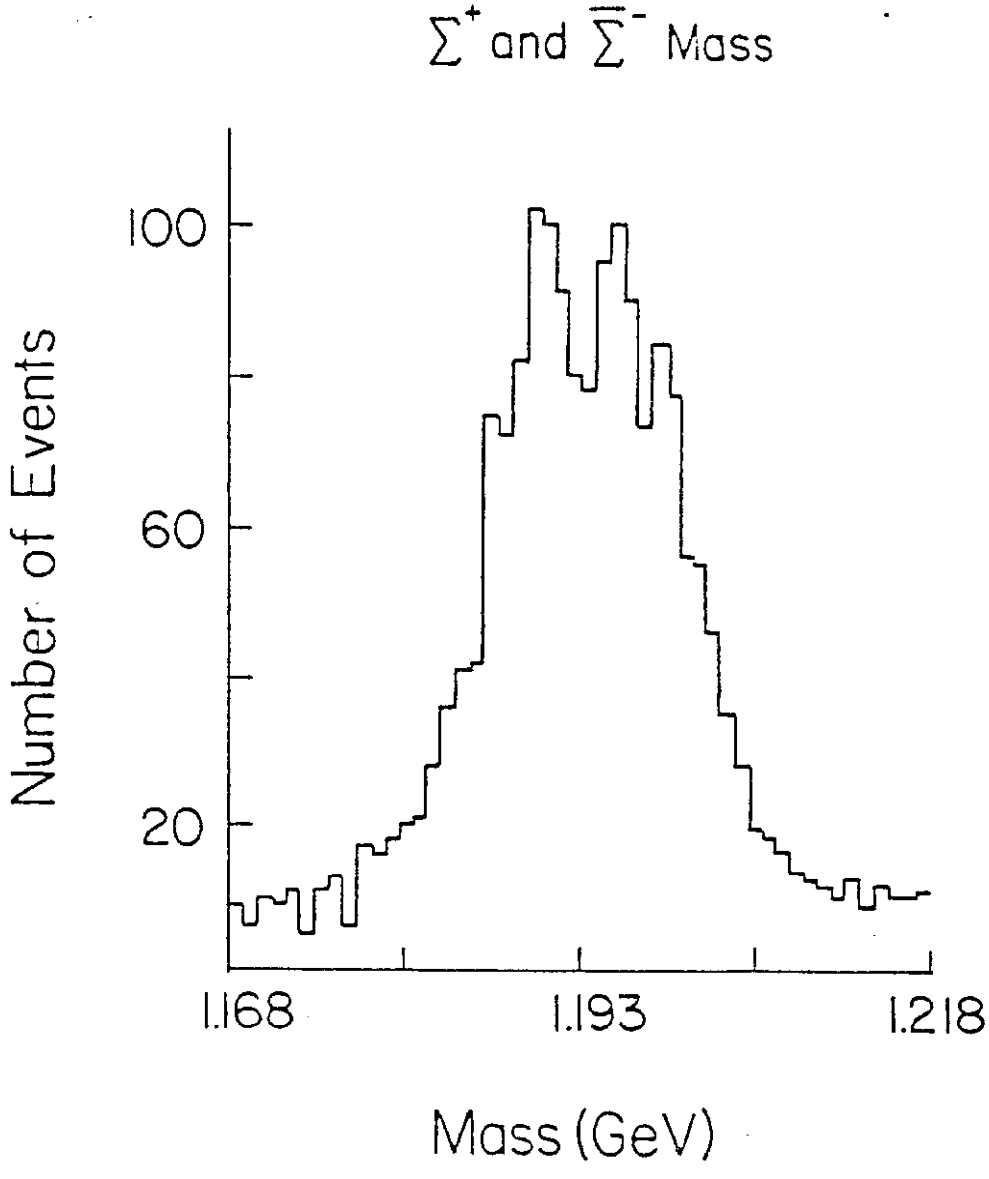
Σ^+ and $\overline{\Sigma}^-$ Mass
Number of Events
100
60
20
1.168
1.193
1.218
Mass (GeV)

Fig. 10

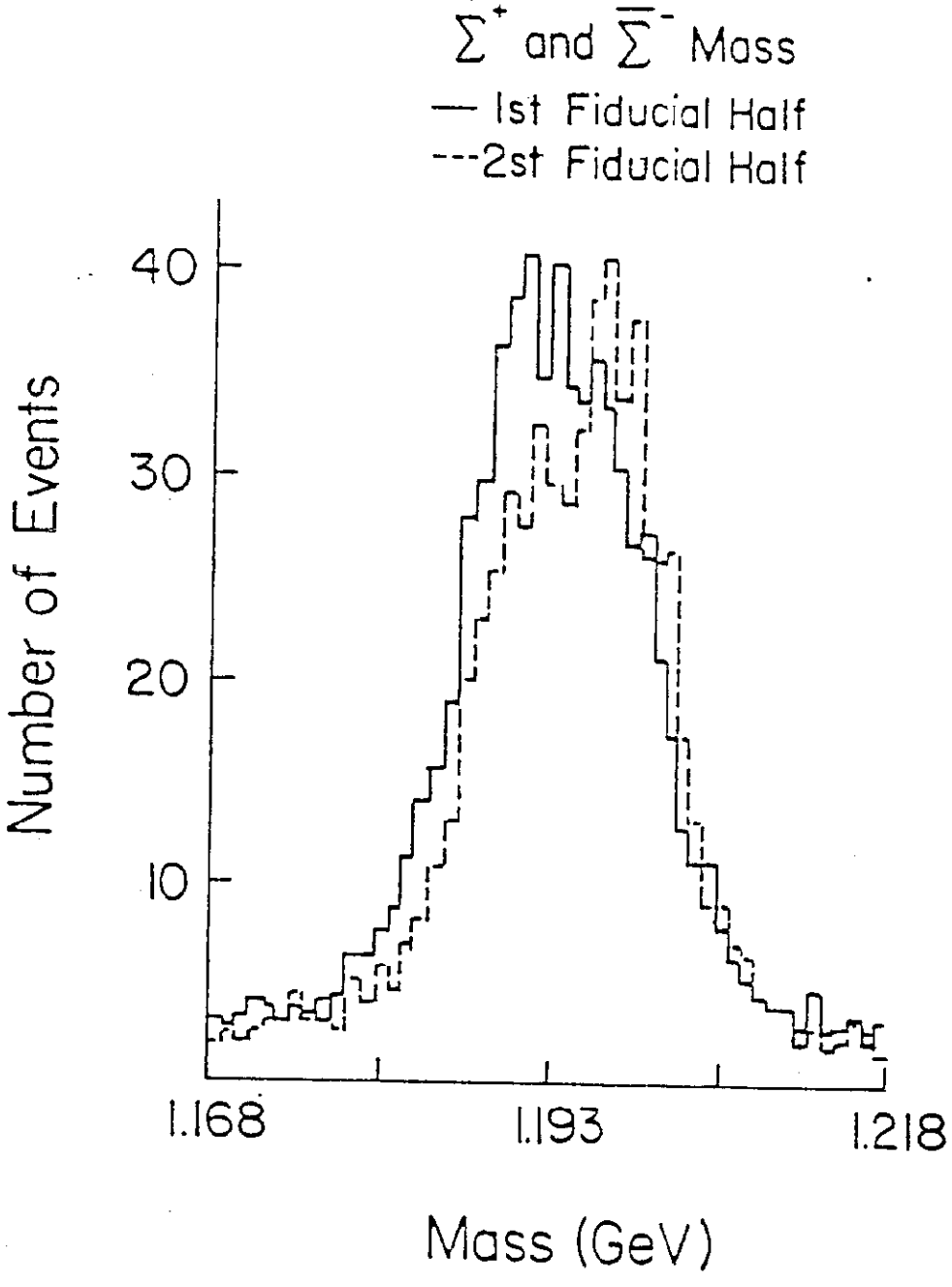
Σ^+ and $\bar{\Sigma}^-$ Mass
— 1st Fiducial Half
---2st Fiducial Half
Number of Events
40
30
20
10
1.168
1.193
1.218
Mass (GeV)

Fig. 11

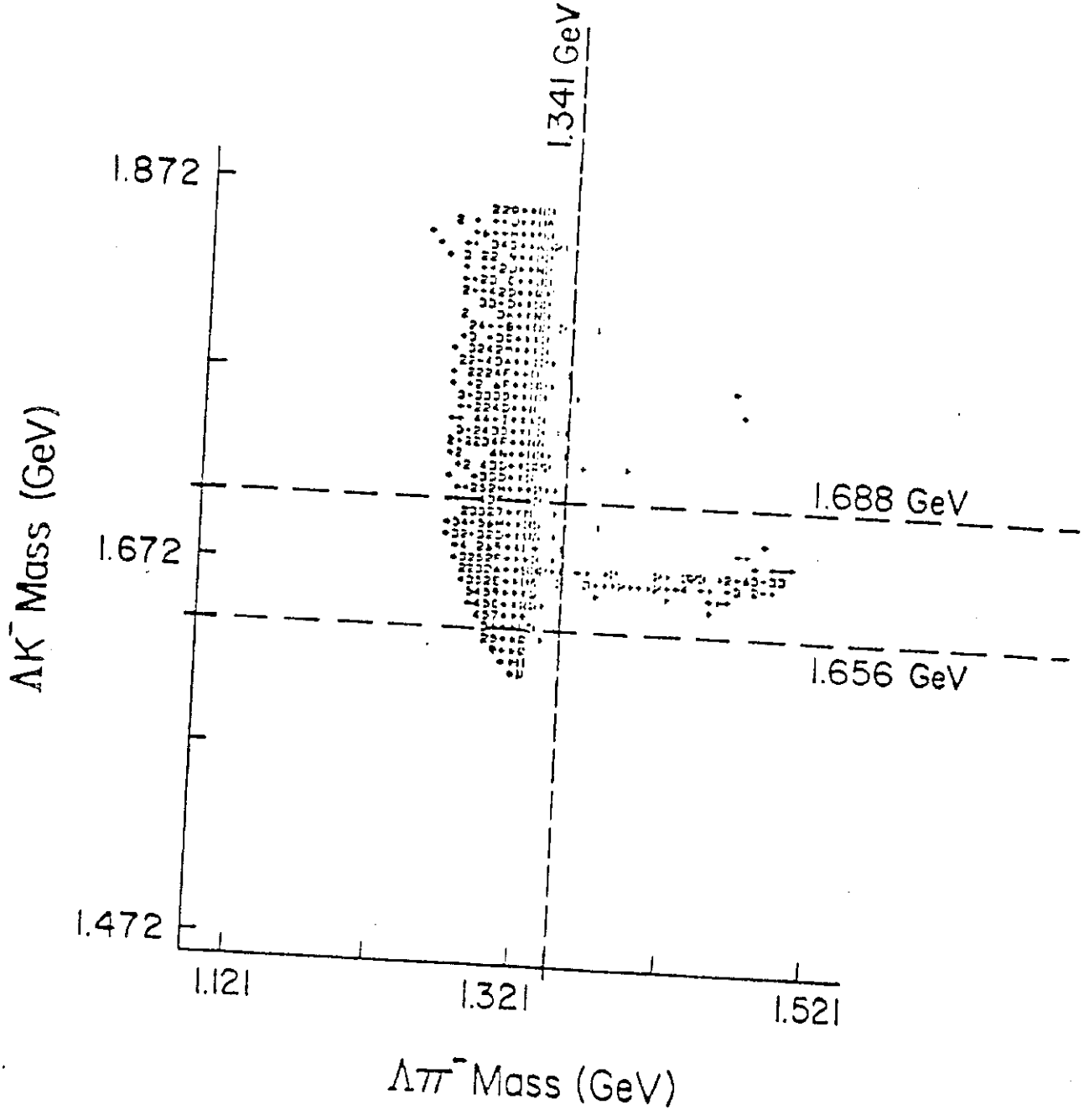
1.341 GeV
1.872
1.688 GeV
1.672
1.656 GeV
1.472
1.121
1.321
1.521
ΛK⁻ Mass (GeV)
Λπ⁻ Mass (GeV)

Fig. 12

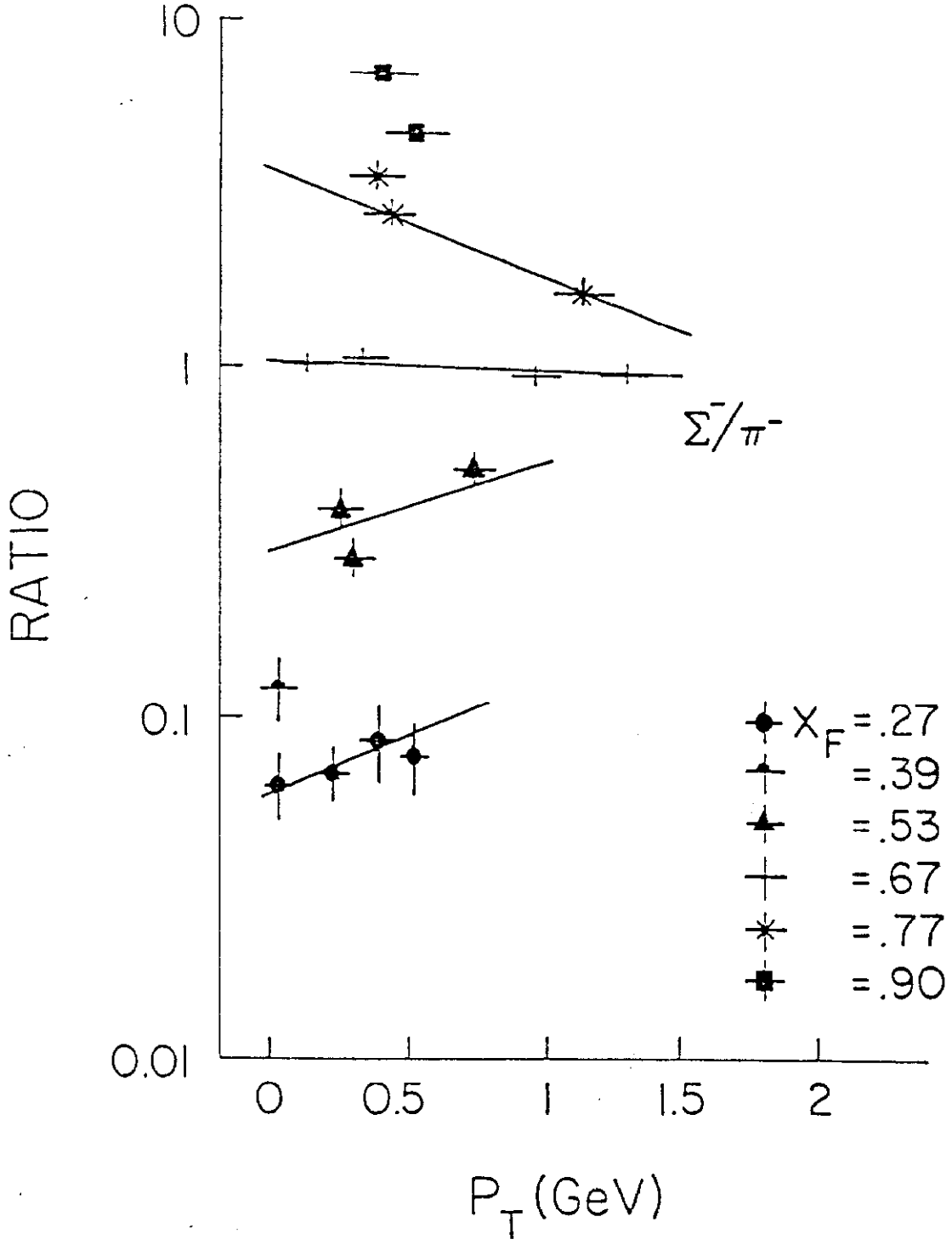

Fig. 13

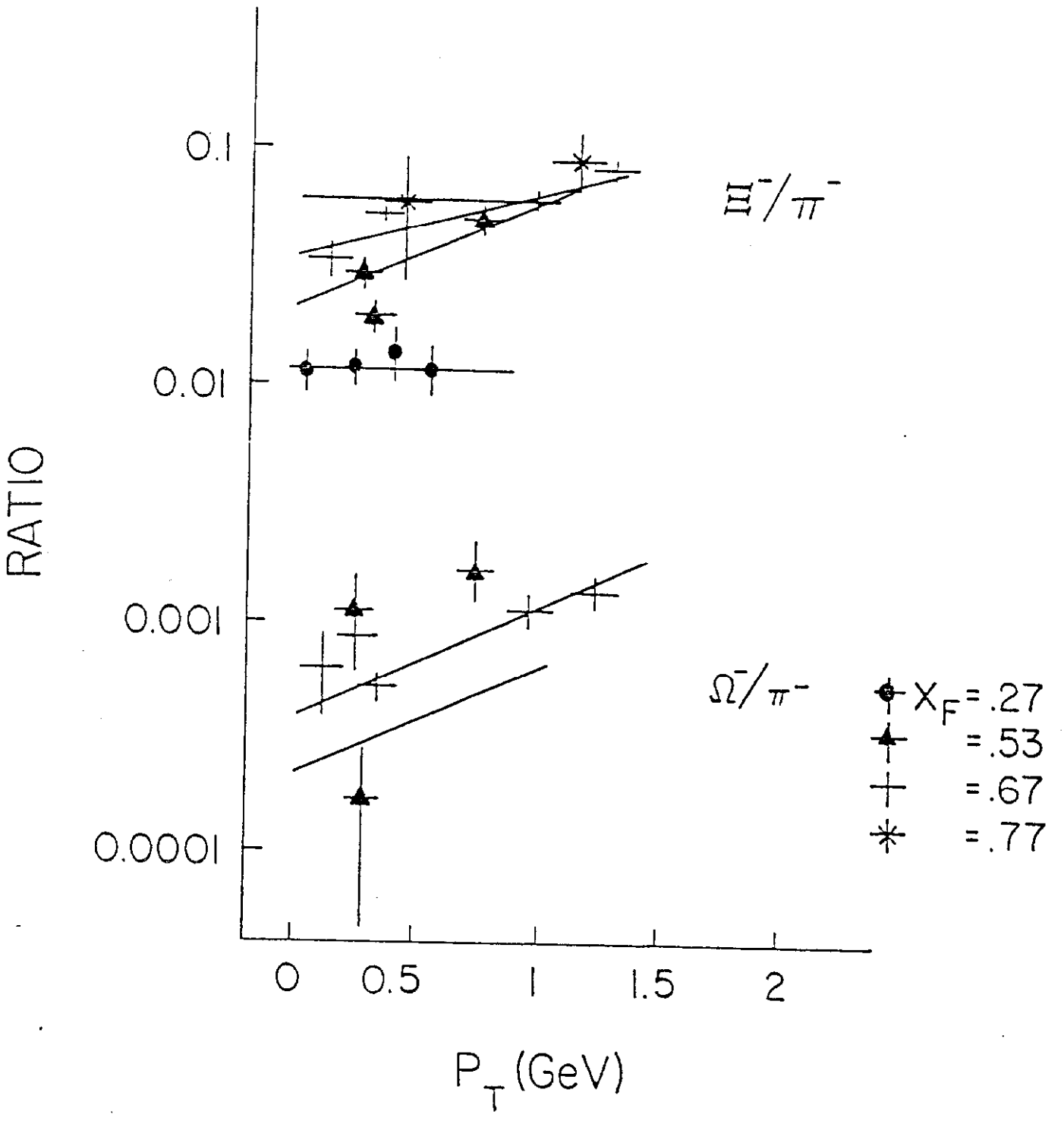
0.1
0.01
0.001
0.0001
RATIO
Ξ^-/π^-
Ω^-/π^-
X_F = .27
= .53
= .67
= .77
0
0.5
1
1.5
2
P_T (GeV)

Fig. 14

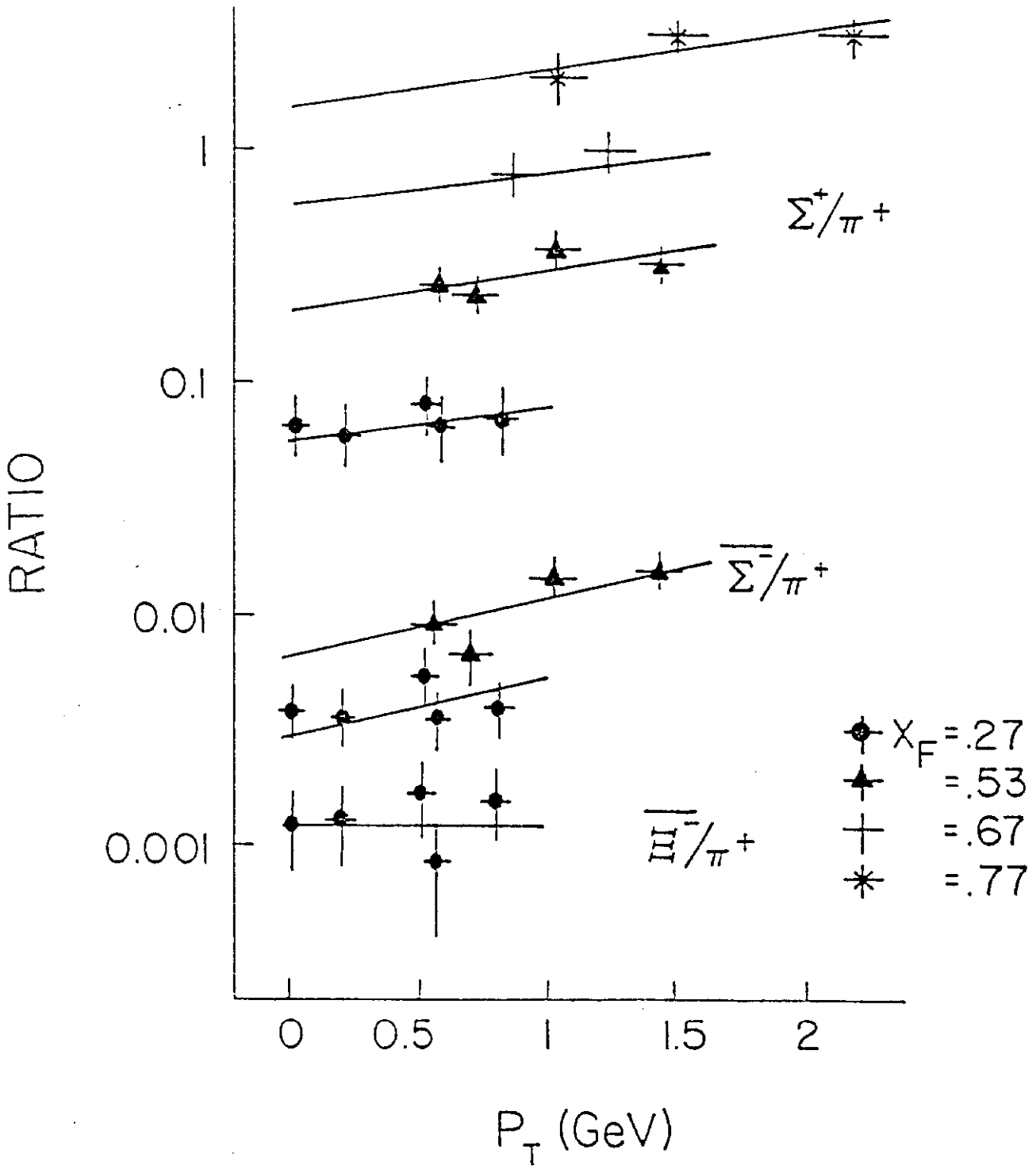
RATIO
1
0.1
0.01
0.001
Σ^+/π^+
$\overline{\Sigma}^-/\pi^+$
$\overline{\Xi}^-/\pi^+$
X_F =.27
=.53
=.67
=.77
0
0.5
1
1.5
2
P_T (GeV)

Fig. 15

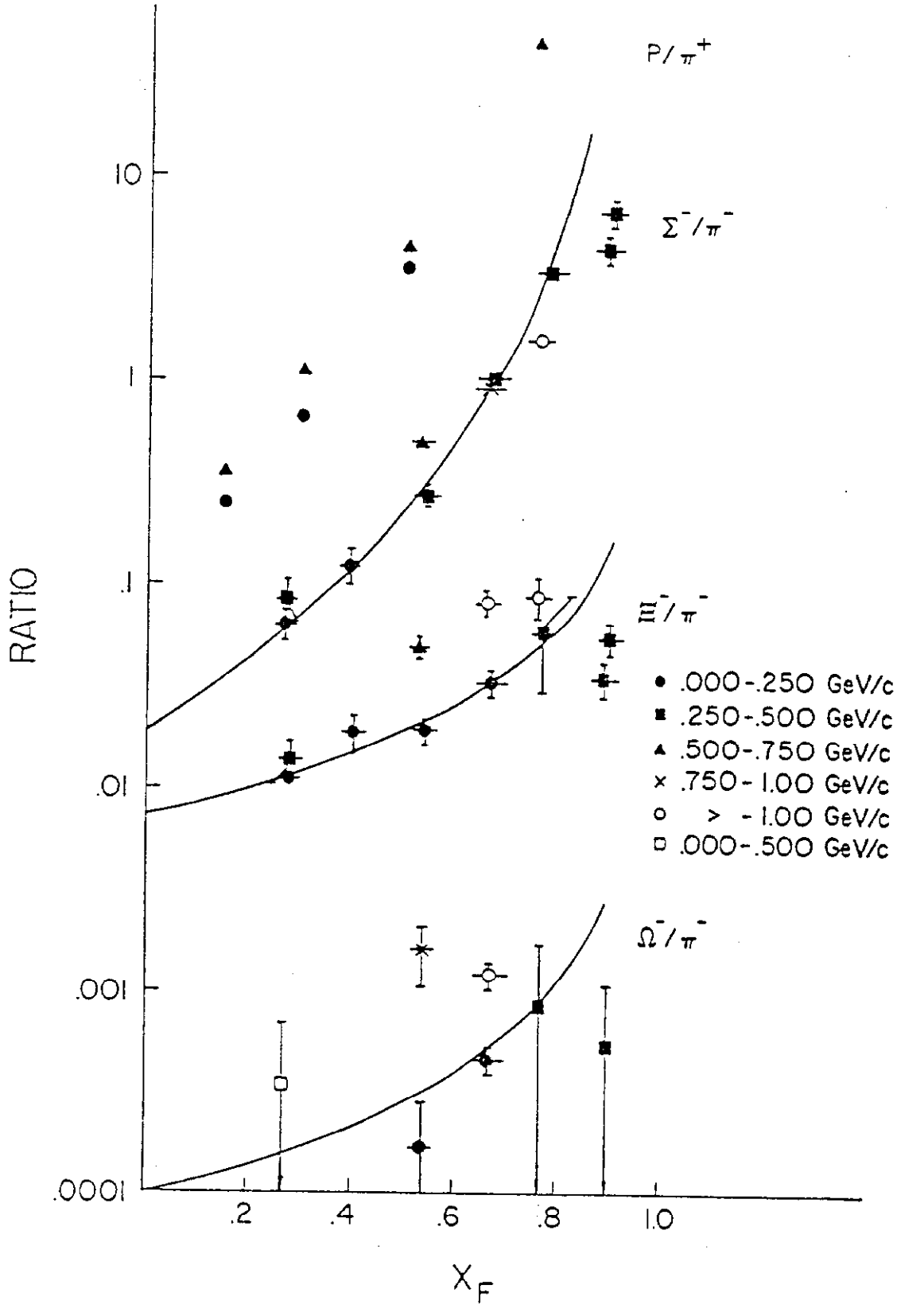
RATIO
10
1
.1
.01
.001
.0001
.2
.4
.6
.8
1.0
X_F
P/π^+
Σ^-/π^-
Ξ^-/π^-
Ω^-/π^-
.000-.250 GeV/c
.250-.500 GeV/c
.500-.750 GeV/c
.750-1.00 GeV/c
> -1.00 GeV/c
.000-.500 GeV/c

Fig. 16

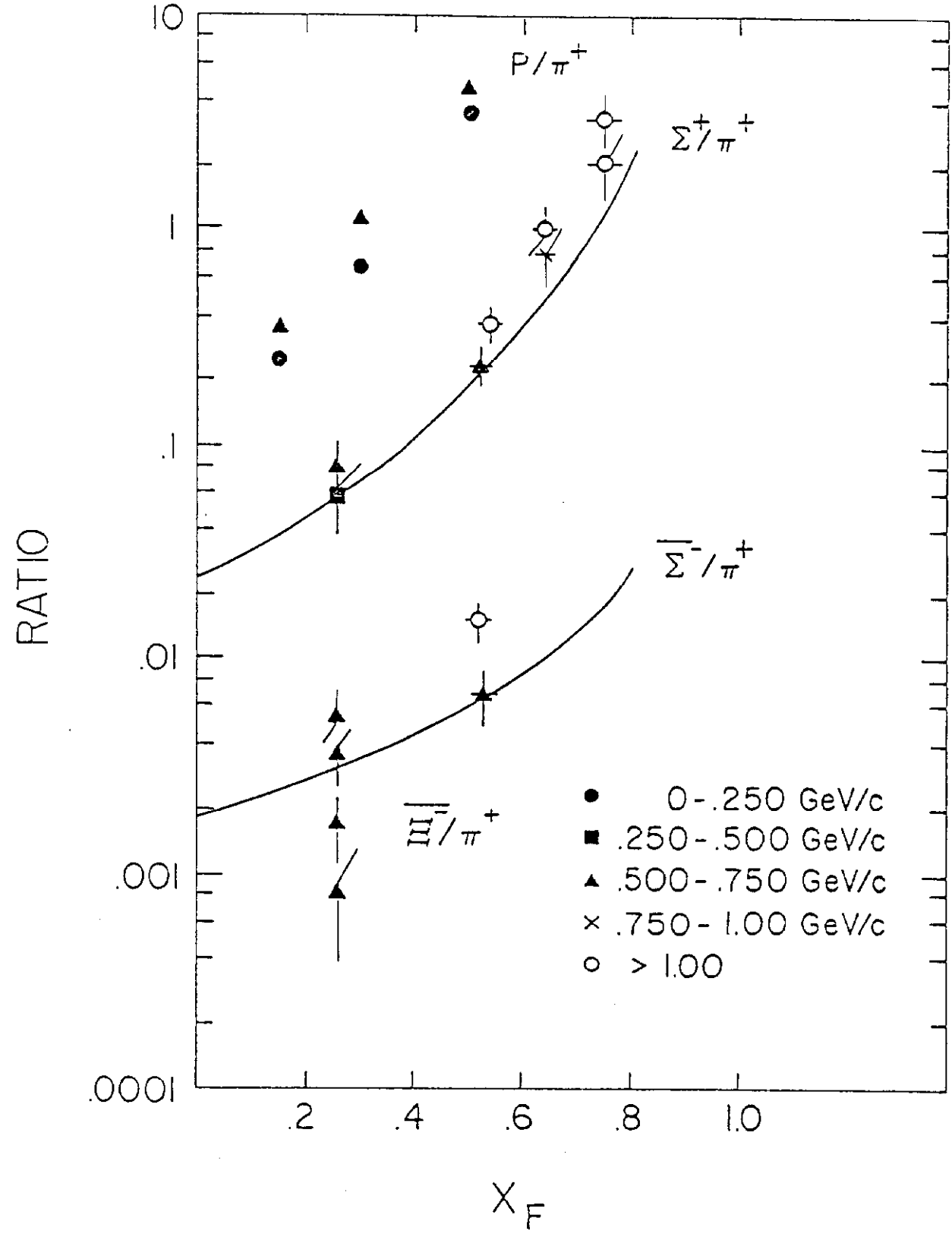
10
1
.1
.01
.001
.0001
RATIO
P/π+
Σ+/π+
Σ̄-/π+
Ξ̄-/π+
0-.250 GeV/c
.250-.500 GeV/c
.500-.750 GeV/c
.750-1.00 GeV/c
> 1.00
.2
.4
.6
.8
1.0
XF

Fig. 17

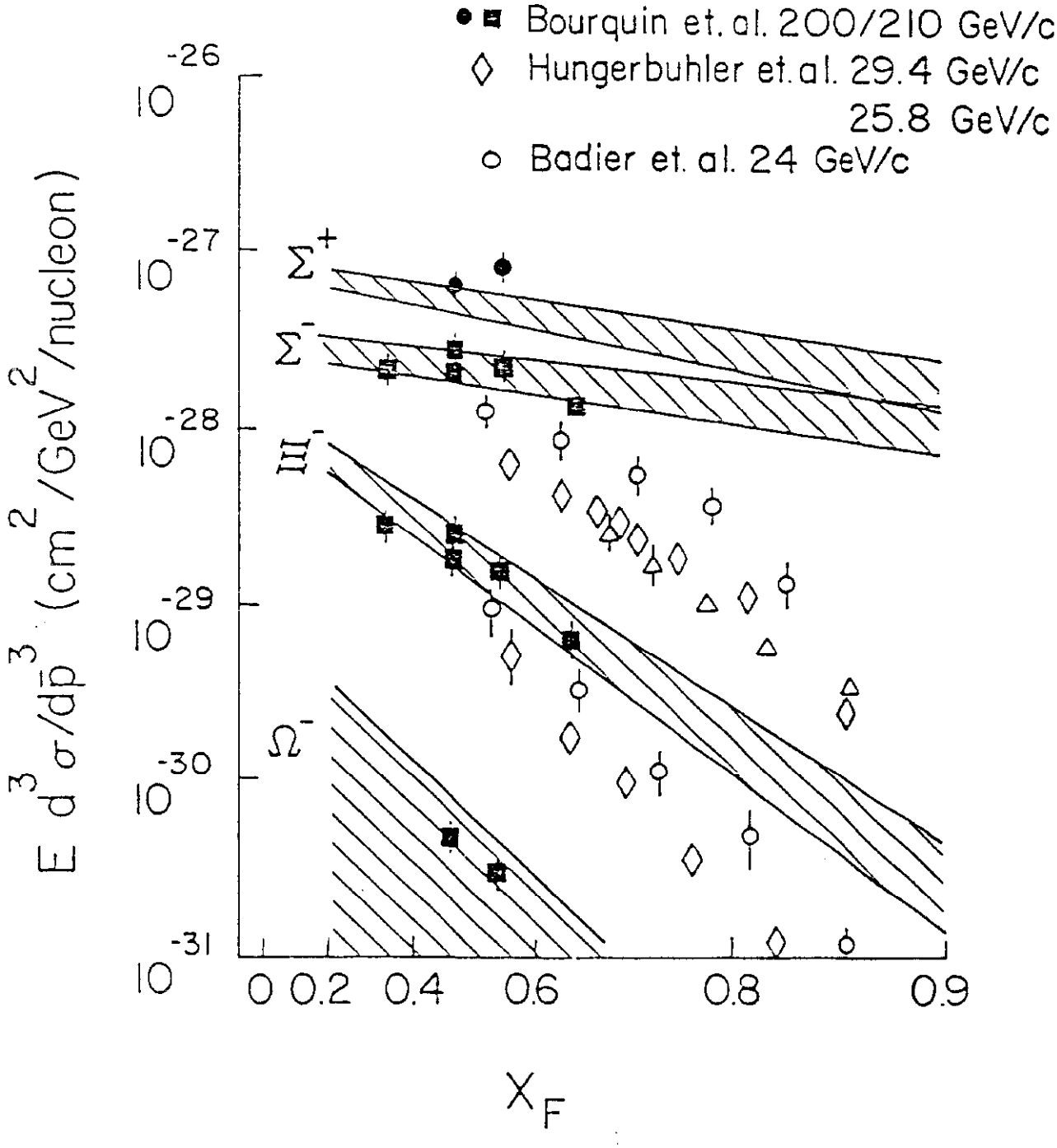
Bourquin et. al. 200/210 GeV/c
Hungerbuhler et. al. 29.4 GeV/c
25.8 GeV/c
Badier et. al. 24 GeV/c
Σ^+
Σ^-
Ξ^-
Ω^-
$E\,d^3\sigma/dp^3$ (cm^2/GeV^2/nucleon)
10^{-26}
10^{-27}
10^{-28}
10^{-29}
10^{-30}
10^{-31}
0 0.2 0.4 0.6 0.8 0.9
X_F

Fig. 18